

Article

Solvothermal Synthesis of g-C₃N₄/TiO₂ Hybrid Photocatalyst with a Broaden Activation Spectrum

Amit Imbar, Vinod Kumar Vadivel  and Hadas Mamane *

Environmental Engineering Program, School of Mechanical Engineering, Faculty of Engineering,
Tel Aviv University, Tel Aviv 69978, Israel

* Correspondence: hadasmg@tauex.tau.ac.il

Abstract: A solvothermal self-made composite of graphitic carbon nitride (g-C₃N₄) and commercially available titanium dioxide (TiO₂) demonstrated the removal of commercial acid green-25 (AG-25) textile dye in a saline water matrix when activated by ultraviolet (UV) and visible light. The g-C₃N₄-TiO₂ composite was characterized by X-ray diffraction (XRD), Nitrogen sorption–desorption recording and modeling by the Brunauer–Emmett–Teller (BET) theory, scanning electron microscopy (SEM), energy-dispersive X-ray spectroscopy (EDX), diffuse reflectance spectroscopy (DRS), X-ray photoelectron spectroscopy (XPS), photoluminescence (PL), and electron spin resonance (ESR). The solvothermal process did not modify the crystalline structure of the g-C₃N₄ and TiO₂ but enhanced the surface area by interlayer delamination of g-C₃N₄. Under a simulated solar spectrum (including UVA/B and vis wavelengths), the degradation rate of AG-25 by the composite was two and four times higher than that of TiO₂ and pure g-C₃N₄, respectively (0.04, 0.02, and 0.01 min^{−1}). Unlike TiO₂, the g-C₃N₄-TiO₂ composite was activated with visible light (the UV portion of the solar spectrum was filtered out). This work provides insight into the contribution of various reactive oxidative species (ROS) to the degradation of AG-25 by the composite.

Keywords: acid dyes; textile dyes; UV–vis activated photocatalyst; graphitic carbon nitride; TiO₂-g-C₃N₄ photocatalyst; solvothermal coupling



Citation: Imbar, A.; Vadivel, V.K.; Mamane, H. Solvothermal Synthesis of g-C₃N₄/TiO₂ Hybrid Photocatalyst with a Broaden Activation Spectrum. *Catalysts* **2023**, *13*, 46. <https://doi.org/10.3390/catal13010046>

Academic Editors: Yongming Fu and Qian Zhang

Received: 13 November 2022

Revised: 19 December 2022

Accepted: 20 December 2022

Published: 26 December 2022



Copyright: © 2022 by the authors. Licensee MDPI, Basel, Switzerland. This article is an open access article distributed under the terms and conditions of the Creative Commons Attribution (CC BY) license (<https://creativecommons.org/licenses/by/4.0/>).

1. Introduction

The textile industry is one of the world's largest industries, providing jobs in low-income countries and playing a vital role in their economy. Over 100,000 synthetic dyes produced annually generate 7×10^5 tons of dyes [1,2]. The textile industry consumes large amounts of water and mainly contributes to wastewater production [3]. Due to process inefficiency, 10–15% of the dyes are washed out into sewer or water reservoir [4]. Synthetic dyes in water reservoirs pose a toxic threat to living organisms and vegetation [5] and hinder photosynthesis by blocking light penetration and increasing biological oxygen demand (BOD) [6,7]. Physical separation methods used in wastewater treatment (such as filtration and sorption) transfer the dyes from the water to a solid phase [8], biodegradation is generally inefficient in dye removal, and the use of oxidants (such as chlorine and ozone) is expensive [4,8]. Advanced oxidation processes (AOPs) are based on reactive oxygen treatment technologies aimed at degrading recalcitrant organic compounds in water through reaction with highly reactive species formed from O₂ as hydroxyl radical (OH·) and superoxide (O₂[−]) that breakdown the organic compounds [9]. Specifically, photocatalysis is of high potential due to the complete removal of organic compounds [10] and the capability to avoid by-products and can be executed without consuming chemicals. The main drawback of photocatalysis is the requirement for intensive energy and light for activation which plays a crucial role in the photocatalytic efficiency and applicability.

The use of TiO₂ in water treatment has been extensively reported in the literature; it is inexpensive, non-toxic, and chemically stable [11–15]. Its main drawbacks are the high

recombination rate of electron-hole (e^-/h^+) pairs and wide band gap (BG), ≥ 3.0 eV. This BG allows electron excitation only by UV wavelengths, making solar light inefficient as only 4% of the solar spectrum lies in the UV spectrum [16,17], making the process energy intensive [18,19].

Coupling photocatalysts to form heterojunctions is a known method for improving photocatalytic activity (PCA) and energy efficiency [20]. Graphitic carbon nitride ($g\text{-C}_3\text{N}_4$) gained interest due to its photocatalytic (PC) properties (BG of 2.7 eV), biocompatibility, low cost and easy production. $g\text{-C}_3\text{N}_4$ combined with TiO_2 showed improved PCA [21–27] while allowing a broader range of solar spectrum use.

In the past decades, many reports of photocatalysts have been published. However, they mainly focused on pure contaminants in de-ionized (DI) water matrices and pure dyes. These conditions are far from the purity of the dyes used in textile dyeing and the water quality of the effluent discharged. At the same time, the existence of other ions is proved to be harmful in photocatalysis [28]. This study demonstrates the solvothermal coupling method of TiO_2 and $g\text{-C}_3\text{N}_4$ for PC degradation of a commercial AG-25, a textile dye used for fabric coloring in a saline water matrix, imitating the salinity and electrical conductivity of dye house effluents.

2. Results and Discussion

2.1. X-ray Diffraction (XRD) Analysis

X-ray diffraction (XRD) analysis is a technique used in materials science to determine the crystallographic structure of a material. The prepared PC composite ($g\text{-C}_3\text{N}_4/\text{TiO}_2$) was analyzed by an XR diffractometer. The clear, sharp peaks of the diffraction pattern and low background noise indicate that the obtained product is of high purity. The resulting sharp peaks in Figure 1 reveal major intensive diffraction peaks for TiO_2 at 25.6° , corresponding to the (111) planes, confirming that the crystalline structure matches the anatase phase of TiO_2 , as analyzed using JCPDS [29]. The graphitic carbon nitride has major intensive peaks at 12.3° and 26.7° , corresponding to the (100) and (002) planes as reported by Miranda et al. [24]. These are attributed to the planar, which repeats the cell structure and sandwich stack reflection of $g\text{-C}_3\text{N}_4$. After compositing with TiO_2 , the significant peaks of $g\text{-C}_3\text{N}_4$ still had decreased peak intensity. Thus, the generation of $g\text{-C}_3\text{N}_4/\text{TiO}_2$ nanostructures can confirm by these structural characterizations.

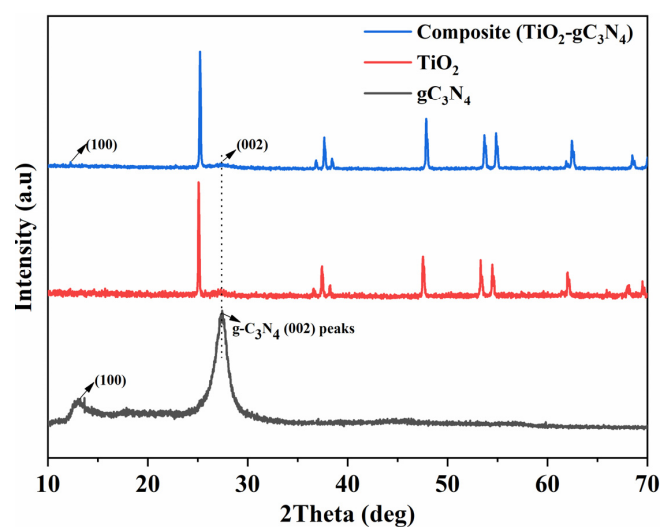


Figure 1. XRD patterns of the composite, TiO_2 and $g\text{-C}_3\text{N}_4$.

2.2. Brunauer-Emmett-Teller (BET) Analysis

Adsorption and desorption experiments were carried out at 77 K, and N_2 isotherms were applied to calculate the specific surface area. The surface area, pore size, and volume

distribution of the $g\text{-C}_3\text{N}_4/\text{TiO}_2$ composite were measured by the multi-point BET and BJH (Barrett, Joyner, and Halenda) method. As shown in Figure S3, mesoporous $g\text{-C}_3\text{N}_4/\text{TiO}_2$ nanostructures are evident with an estimated pore volume of 0.039 cc/g , pore radius of $\sim 2.038\text{ nm}$, and pore size of 4.08 nm . As shown in Figure S4, the $g\text{-C}_3\text{N}_4/\text{TiO}_2$ composite shows a hysteresis loop with a type H3 shape and shifts at high relative pressures (P/P_0) between 0.8 and 1.0, which suggests a mesoporous structure. Mesoporosity is typical of wrinkled, sheetlike particles, and this result is consistent with SEM images [30]. The surface area was $15.43\text{ m}^2\text{ g}^{-1}$, higher than obtained in our previous study (Kumar et al. [31]) for sole $g\text{-C}_3\text{N}_4$ after solvothermal treatment. The different results are possibly rooted in the large amount of TiO_2 in the composite, which is smaller than $g\text{-C}_3\text{N}_4$, as shown in Figure 2.

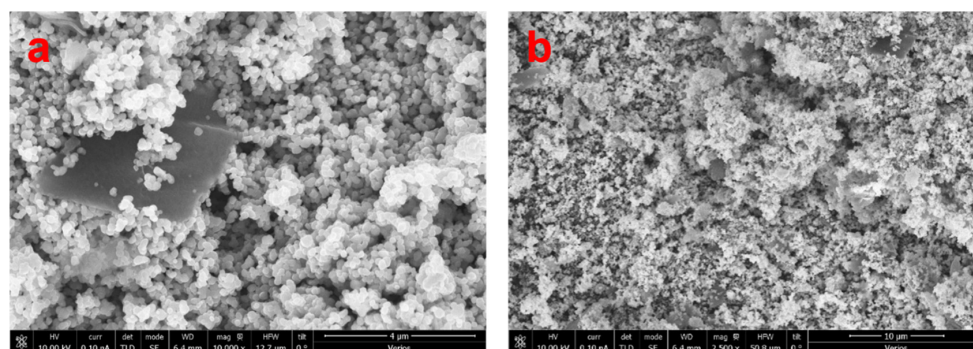


Figure 2. SEM images of the composite. (a) magnification of 10^4 and (b) magnification of 2500.

2.3. Scanning Electron Microscopy (SEM)

EDX analysis was performed to obtain the composite composition. Figures S5–S7 show that the sheet-shaped particles are primarily composed of carbon and nitrogen, while the sphere-shaped particles are composed mainly of titanium and oxygen. The composition and the shape of the sheet-shaped particles both confirm that these particles are of $g\text{-C}_3\text{N}_4$. In contrast, the composition of the spherical particles is that of TiO_2 .

The SEM images of as-synthesized $g\text{-C}_3\text{N}_4/\text{TiO}_2$ structures are presented in Figure 2. After compositing TiO_2 with $g\text{-C}_3\text{N}_4$, TiO_2 nanoparticles uniformly adhered to $g\text{-C}_3\text{N}_4$. However, $g\text{-C}_3\text{N}_4$ has a wrinkled sheetlike morphology, as reported in former publications [31–33], whereas TiO_2 has smaller and sphere-shaped particles. $g\text{-C}_3\text{N}_4$ has a crystalline structure similar to the solvothermal-treated $g\text{-C}_3\text{N}_4$ and contrary to the untreated $g\text{-C}_3\text{N}_4$ [31]. This combination could promote the charge transfer between $g\text{-C}_3\text{N}_4$ and TiO_2 by the Z-scheme route [30], as demonstrated in Figure 3.

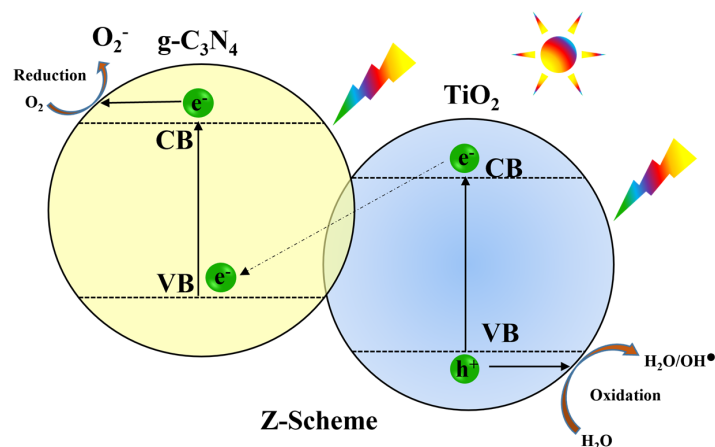


Figure 3. Z-scheme of TiO_2 and $g\text{-C}_3\text{N}_4$.

2.4. Absorption Spectrum and DRS Analysis

UV–vis diffuse reflectance spectra were recorded to probe the prepared photocatalysts' optical properties. As shown in Figure S8b, the absorption edges of g-C₃N₄, TiO₂ and the composite are located at approximately 389, 334 and 340 nm, respectively. Compared to TiO₂, the absorption edge positions of the composite exhibited a red shift toward the visible range alongside an extension of the absorbance spectrum toward ~430 nm wavelengths due to the g-C₃N₄ introduction with TiO₂ [34]. Furthermore, the band gaps of photocatalysts could be determined by the following equation:

$$\alpha h\nu = A(h\nu - E_g)^{n/2} \quad (1)$$

where α , A , h , ν , and E_g represent the absorption coefficient, proportionality constant, Planck constant, light frequency, and band gap energy, respectively [35]. A plot based on the Kubelka–Munk function (Equation (1)) versus the energy of light is shown in Figure S8a. The estimated band gap values of the photocatalysts are about 2.80, 2.86, and 3.19 eV for g-C₃N₄, composite, and TiO₂, respectively. The composite shows a narrower BG than TiO₂ and is slightly wider than g-C₃N₄. As the band gap increases, the recombination of e⁻/h⁺ pairs decreases, enhancing the ROSs production, and the narrowing of the BG (compared with TiO₂) enables activation by the visible-light region. Therefore, the UV–vis diffuse reflectance spectroscopy (DRS) results indicated more photogenerated charges when activating the composite are excited under UV–vis spectrum irradiation, which enhances their photocatalytic performance [36].

2.5. X-ray Photoelectron Spectroscopy (XPS)

Figure 4 shows the XPS spectra of g-C₃N₄, TiO₂ and the composite. The full XPS spectrum presented all the peaks (C 1s, N 1s, Ti 2p, O 1s) of g-C₃N₄, TiO₂ plus composite (TiO₂/g-C₃N₄) nanomaterials. Thus, the generation of g-C₃N₄/TiO₂ nanostructures can be confirmed by these structural characterizations and well supports the XRD analysis in Figure 1. However, the in the valence band (VB) of TiO₂ and g-C₃N₄ is directly excited to its conduction band (CB) by absorbing photons with energy higher than or equal to its energy gap (E_g) and meanwhile resulting in the generation of a positive hole in the VB. Compared to typical photocatalysts such as TiO₂, g-C₃N₄ has the most negative CB value of −1.69 eV versus the normal hydrogen electrode (NHE) and a neutral band gap (~3.19 eV), summarized in Table S2. Furthermore, a detailed analysis of the XPS valence band spectra confronted with band structure calculations was achieved for the three photocatalysts TiO₂, g-C₃N₄ and composite (TiO₂/g-C₃N₄). Furthermore, through valence band spectra analysis, conduction band offset (−0.63 eV) and valence band offset (2.23 eV) of g-C₃N₄–TiO₂ heterojunction were estimated (Figure S9). The band gap (ECB) and valence band (EVB) positions of the photocatalyst materials can be calculated by the following equations:

$$E_{CB} = X - E_C - \frac{1}{2}E_g \quad (2)$$

$$E_{VB} = E_{CB} + E_g \quad (3)$$

where E_{VB} and E_{CB} represent the valence band and conduction band position of the semiconductor material, E_C is the hydrogen electron free energy (4.5 eV), and X represents the electronegativity of the semiconductor material.

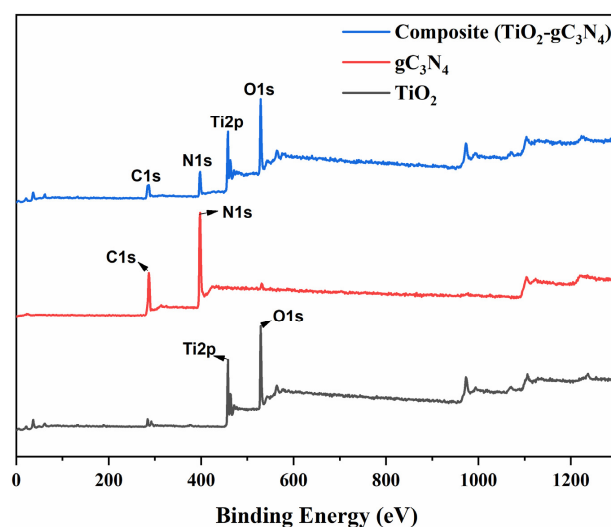


Figure 4. Full XPS spectrum presented all the peaks (C 1s, N 1s, Ti 2p, O 1s) of g-C₃N₄, TiO₂ and the composite (TiO₂/g-C₃N₄) nanomaterials.

2.6. Photo Luminescence (PL)

Figure 5 shows PL of g-C₃N₄, TiO₂ and the composite. The spectrum shows emission at 350 nm corresponding to the recombination of e⁻/h⁺ pairs, with the intensity directly proportional to the photogenerated e⁻/h⁺ recombination in the catalyst. The composite's intensity is between the two substances of origin, a decrease in intensity was obtained with the composite compared with g-C₃N₄ and increased intensity compared with TiO₂.

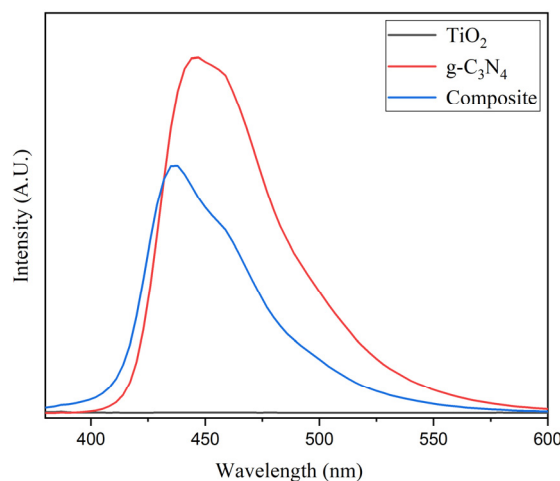


Figure 5. PL spectra of g-C₃N₄, TiO₂ and the composite.

2.7. Electron Spin Resonance Spectroscopy (ESR)

The production of ROSs by the g-C₃N₄, TiO₂ and the composite under solar light was studied by ESR spin trap experiments. Aqueous suspensions of each catalyst were irradiated separately under solar light in the presence of 5-methyl-1-pyrroline N-oxide (BMPO), which traps both hydroxyl and superoxide radicals. To distinguish the signal corresponding to hydroxyl radical, dimethyl sulfoxide (DMSO), a hydroxyl radical scavenger, was added to the catalysts-BMPO suspensions.

The resulting signals are shown in Figure 6. When only BMPO is present, the signals show the formation of ROSs (either OH· or O₂⁻) by the irradiation of all three substances. The composite's signals almost utterly correspond to those of BMPO-OOH, implying that it produces superoxide radicals. The consistent intensity of the signal suggests that the composite does not produce hydroxyl radicals.

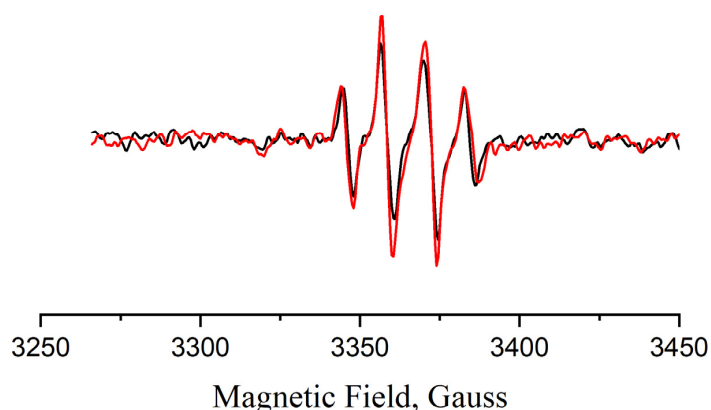


Figure 6. BMPO-OOH with (red line) and without (black line) DMSO signal from the suspension of the composite.

2.8. Photocatalytic Degradation of AG-25 under Solar Irradiation in Saline Water

10-ppm AG-25 in saline water matrix was used as a target pollutant to study the degradation by the catalysts. The catalyst was stirred in the solution for 30 min (time -30 to 0) under dark conditions for sorption control, followed by simulated solar irradiation for 90 min (time 0 to 90). Under dark conditions, 16, 12, and 11% removal of AG-25 were observed by the composite, $g\text{-C}_3\text{N}_4$, and TiO_2 , respectively. The composite has an increased surface area, as mentioned in Section 3.2, promoting higher sorption over the catalyst.

Figure 7 shows the degradation rate of AG-25 by the three catalysts. AG-25 total removal by $g\text{-C}_3\text{N}_4$, TiO_2 , and the composite were 59, 86, and 98%, respectively, implying that all three catalysts can degrade AG-25. The degradation rate of AG-25 using the composite was twice as high as commercially available TiO_2 and four times higher than that of pure $g\text{-C}_3\text{N}_4$. The higher results obtained by TiO_2 and the composite can be explained by the type of radicals formed by the catalyst. TiO_2 primarily produces hydroxyl radicals [37,38], which have higher oxidation potential than superoxide radicals, the main ROS produced by $g\text{-C}_3\text{N}_4$. Moreover, the PL results show significant recombination in $g\text{-C}_3\text{N}_4$ compared with TiO_2 . However, coupling the two catalysts in the composite can form a heterojunction that suppresses the recombination rate and improves photon energy usage, as shown in PL spectra in Figure 5 and the broadened absorption spectrum demonstrated in Figure S8, resulting in enhanced PCA [39].

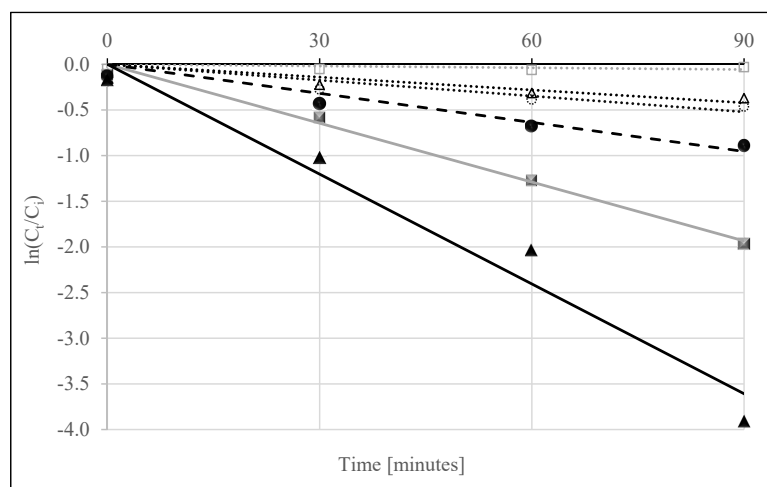


Figure 7. Photocatalytic degradation rate of 100 mL AG-25 10 ppm in brine for 90 min under solar irradiation with (filled shapes) and without (hollow shapes) UV spectrum cutoff by the composite (\blacktriangle , \triangle), $g\text{-C}_3\text{N}_4$ (\bullet , \circ), and TiO_2 (\blacksquare , \square).

Table 1 summarizes the degradation rate and total degradation of each catalyst. Adly et al. [40] degraded AG-25 with graphene oxide/titanium dioxide composites (GO-TiO₂) under UV–vis irradiation, reporting 40% removal (vs. 98% in our work) of AG-25 after 90 min by a similar concentration of catalysts but a higher concentration of AG-25.

Table 1. Total degradation (after 90 min) and degradation rate of AG-25 by coupled and uncoupled g-C₃N₄-TiO₂ under solar irradiation, with and without LP400 filter.

Catalyst	Percent Degradation of AG-25 (%)	Rate of AG-25 Degradation (min ⁻¹) × 10 ⁻³
g-C ₃ N ₄	59%	10.6
TiO ₂	86%	21.5
Composite	98%	40.1
g-C ₃ N ₄ —LP400	37%	5.8
TiO ₂ —LP400	0%	0
Composite—LP400	31%	4.7

2.9. Photocatalytic Degradation of AG-25 under Solar Irradiation in Saline Water with a UV Cutoff

The role of UV and visible light in PCA was examined by degrading 10-ppm AG-25 in saline water under simulated solar irradiation, similar to Section 2.8, with a UV filter for UV cutoff. Figure 8 presents the degradation rate of AG-25 by the composite, g-C₃N₄, and TiO₂ under the visible spectrum. AG-25 degradation by g-C₃N₄, TiO₂, and the composite after 90 min was 37%, 0%, and 31%, respectively, demonstrating that TiO₂ is a UV-driven catalyst. Moreover, a higher g-C₃N₄ ratio in the catalysts resulted in higher visible-based PCA in the absence of UV wavelengths. These results show the composite's versatility as both a UV and a visible light-activated catalyst. In both cases (with and without the LP400 filter), the composite is superior to the commercial TiO₂, while the cutoff results show increased degradation (37% compared with 31% removal) by g-C₃N₄. However, comparing the full spectrum results (without the LP400 filter) shows a clear advantage of the composite over pure g-C₃N₄. Generally, the composite's versatile activation spectrum and improved results under total spectrum irradiation are advantageous.

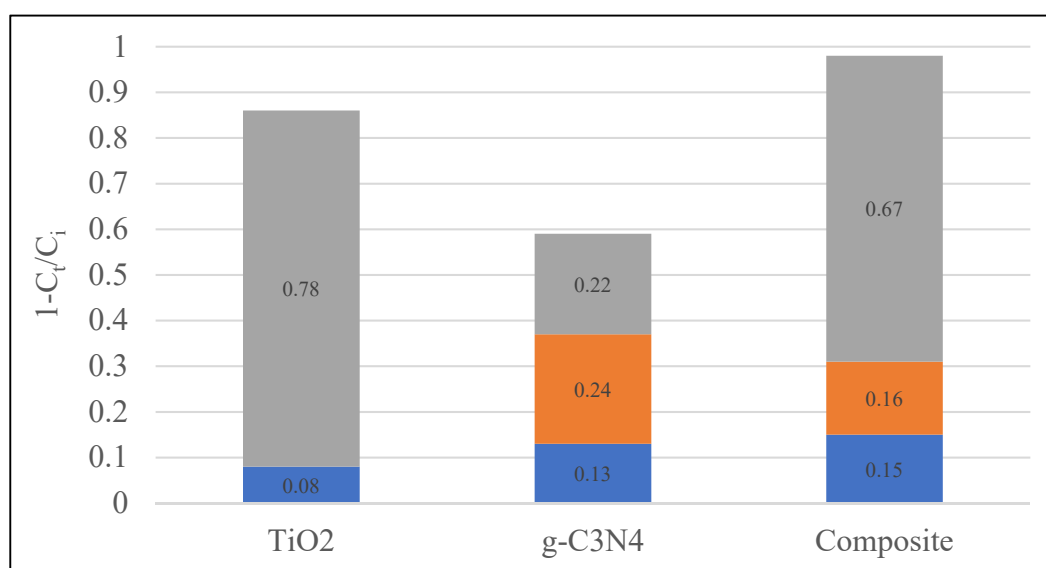


Figure 8. Segmentation of sorption (blue background), visible light (orange background), and UV (grey background) contribution to the total degradation of 100 mL AG-25 10 ppm by TiO₂, g-C₃N₄ and the composite after 90 min irradiation.

3. Materials and Methods

3.1. Materials

Melamine and Titanium dioxide (99% purity) were purchased from Sigma-Aldrich, Darmstadt, Germany.

Acid Green-25 Textile Dye

AG-25, a light green textile acid dye, was provided by Colourtex Industries Ltd., Hamburg, Germany, and has a molecular formula of $C_{28}H_{20}N_2Na_2O_8S_2$. AG-25 stock solution of 300-ppm AG-25 was prepared and diluted with deionized (DI) water to reach a concentration of 10 ppm used for the experiments. The conductivity was adjusted to 36 mS cm^{-1} using NaCl to simulate a real textile dye effluent. Due to AG-25 physical properties, the concentration of AG-25 could be determined by spectroscopic measurement of the visible light spectrum. The maximum absorbance wavelength value of the dye solutions was 614 nm (Evolution 220 UV-Visible spectrophotometer, Thermo Scientific, Waltham, MA, USA) to determine the AG-25 concentration.

The removal of AG-25 was calculated using Equation (4).

$$\text{AG-25 Removal} = (C_i - C_t)/C_i \quad (4)$$

Here, C_i stands for the initial concentration, and C_t stands for concentrating the samples.

3.2. Characterization

The $TiO_2/g-C_3N_4$ powder crystalline structure was characterized by a D8 Advance diffractometer (Bruker AXS, Karlsruhe, Germany) with a secondary graphite monochromator, 2° Soller slits, and a 0.2 mm receiving slit. Low-background quartz sample holders were carefully filled with the powdered samples. The nanoparticle morphology and average particle size were further investigated by a Quanta 200 FEG environmental scanning electron microscope equipped with a field-emission electron gun (FEG). The samples were coated with a conductive carbon grid and imaged in a Hitachi S3200N SEM-EDS system at 20 kV accelerating voltage. The surface area, pore size and volume distribution of the modified and unmodified $g-C_3N_4$ were measured by N_2 adsorption-desorption and the BJH (Barrett, Joyner, and Halenda) method, respectively. To probe the optical properties of the prepared photocatalysts, UV-visible diffuse reflectance spectra were recorded using a UV-Vis-NIR spectrophotometer (Cary 5000 + UMA, Agilent, Santa Clara, CA, USA).

3.3. Preparation of $g-C_3N_4$

$g-C_3N_4$ was synthesized via the thermal-condensation method. In short, 4 g melamine (Sigma-Aldrich, 99%) was heated to 540°C in a packed aluminum crucible under ambient pressure in the air for 2 h with a heating rate of $15^\circ\text{C min}^{-1}$ in a muffle furnace. The resultant powder reached room temperature and was washed with acetone.

3.4. Solvothermal Method

TiO_2 and $g-C_3N_4$ (named composite) were coupled via the solvothermal method. The $TiO_2-g-C_3N_4$ mixture (2:1 ratio, 1 g) was stirred for 3 h in ethanol (70%) in a 50 mL PTFE pressure-tight liner at $\sim 65^\circ\text{C}$. Subsequently, the PTFE liner was placed in a stainless-steel jacket and heated to 180°C for 10 h. The resulting catalyst was filtered and dried before usage.

3.5. Photocatalytic Degradation of AG-25 in Saline Water

The PC experiments were conducted under a 300-W solar simulator, ozone-free xenon arc lamp (Newport full-spectrum, $50.8 \text{ mm} \times 50.8 \text{ mm}$, Irvine, CA USA) equipped with a 1.5 Global Air Mass filter to remove infrared light, as shown in Figure S1. The xenon lamp's incident spectral irradiance and photon fluence are recorded by a spectroradiometer (International Light, ILT 900R, Peabody, MA, USA), as in Figure S2. The integrated

incident irradiance was 2.865 and 62.737 mW cm⁻² for the UV (280–400 nm) and visible (400–1251 nm) ranges, respectively.

The PC experiments were conducted using AG-25 (100 mL, 10 ppm) in a crystalline cylinder (70 × 50 mm). The powdered catalyst (500 ppm) was sonicated and added to the AG-25 solution under stirring. The solution was constantly mixed under dark conditions for 30 min, followed by 90 min under solar-like irradiation. Samples of the slurry solution were taken in 30 min intervals and centrifuged (14600 RPM, 10 min) to separate the catalyst from the solution. The samples were analyzed in a spectroradiometer (Evolution 220 UV–Visible spectrophotometer, Thermo Scientific) to determine the AG-25 concentration.

3.6. Photocatalytic Degradation of AG-25 with UV Cutoff—LP400

Distinguishing between PCA driven by visible light and UV irradiation was performed similarly to as in Section 2.5, using a UV filter (400 HLP/130 mm, OMEGA OPTICAL, Brattleboro, VT, USA) to block UV wavelengths (i.e., $\lambda < 400$ nm) from reaching the slurry.

4. Conclusions

The composite showed improved photocatalytic activity compared with TiO₂ and g-C₃N₄ under solar irradiation. As demonstrated by the BET results, the solvothermal method increased the surface area resulting in increased photocatalytic activity relative to the origin catalysts, reflected in the enhanced degradation rate of AG-25. The UV cutoff experiments showed a versatile spectrum ranging from UV to the visible spectrum, allowing composite activation at various wavelengths. This study provides a simple synthesis method of a composite that can efficiently remove acid-dye effluents in a versatile spectrum of wavelengths.

Supplementary Materials: The following supporting information can be downloaded at: <https://www.mdpi.com/article/10.3390/catal13010046/s1>, Figure S1: Newport solar simulator, Figure S2: Spectral incident irradiance, Figure S3: Pore size distribution and volume curves, Figure S4: BET sorption\desorption curves, Figures S5–S7: EDX elemental analysis, Figure S8: UV–visible DRS spectra, Figure S9: XPS, S10:ESR, Table S1: XRD, Table S2: XPS.

Author Contributions: Supervision, reviewing and project administration, H.M.; methodology, V.K.V.; investigation, V.K.V. and A.I.; writing—original draft, A.I.; writing—review and editing, H.M., V.K.V. and A.I. All authors have read and agreed to the published version of the manuscript.

Funding: This research received no external funding.

Data Availability Statement: The data presented in this study are available on request from the corresponding author.

Conflicts of Interest: The authors declare no conflict of interest.

References

1. Ajmal, A.; Majeed, I.; Malik, R.N.; Idriss, H.; Nadeem, M.A. Principles and mechanisms of photocatalytic dye degradation on TiO₂ based photocatalysts: A comparative overview. *RSC Adv.* **2014**, *4*, 37003–37026. [[CrossRef](#)]
2. Ananthashankar, A.G.R. Production, Characterization and Treatment of Textile Effluents: A Critical Review. *J. Chem. Eng. Process Technol.* **2013**, *5*, 1–18. [[CrossRef](#)]
3. Arami, M.; Limaee, N.Y.; Mahmoodi, N.M. Evaluation of the adsorption kinetics and equilibrium for the potential removal of acid dyes using a biosorbent. *Chem. Eng. J.* **2008**, *139*, 2–10. [[CrossRef](#)]
4. Natarajan, S.; Bajaj, H.C.; Tayade, R.J. Recent advances based on the synergetic effect of adsorption for removal of dyes from waste water using photocatalytic process. *J. Environ. Sci.* **2018**, *65*, 201–222. [[CrossRef](#)] [[PubMed](#)]
5. Chung, K.T. Azo dyes and human health: A review. *J. Environ. Sci. Heal.—Part C Environ. Carcinog. Ecotoxicol. Rev.* **2016**, *34*, 233–261. [[CrossRef](#)]
6. Gita, S.; Hussan, A.; Choudhury, T.G. Impact of Textile Dyes Waste on Aquatic Environments and its Treatment. *Environ. Ecol.* **2017**, *35*, 2349–2353.
7. Holkar, C.R.; Jadhav, A.J.; Pinjari, D.V.; Mahamuni, N.M.; Pandit, A.B. A critical review on textile wastewater treatments: Possible approaches. *J. Environ. Manag.* **2016**, *182*, 351–366. [[CrossRef](#)]

8. Rajeshwar, K.; Osugi, M.E.; Chanmanee, W.; Chenthamarakshan, C.R.; Zaroni, M.V.B.; Kajitvichyanukul, P.; Krishnan-Ayer, R. Heterogeneous photocatalytic treatment of organic dyes in air and aqueous media. *J. Photochem. Photobiol. C Photochem. Rev.* **2008**, *9*, 171–192. [[CrossRef](#)]
9. Thiruvenkatachari, R.; Vigneswaran, S.; Moon, I.S. A review on UV/TiO₂ photocatalytic oxidation process. *Korean J. Chem. Eng.* **2008**, *25*, 64–72. [[CrossRef](#)]
10. Liu, C.; Mao, S.; Shi, M.; Wang, F.; Xia, M.; Chen, Q.; Ju, X. Peroxymonosulfate activation through 2D/2D Z-scheme CoAl-LDH/BiOBr photocatalyst under visible light for ciprofloxacin degradation. *J. Hazard. Mater.* **2021**, *420*, 126613. [[CrossRef](#)]
11. Ajmal, A.; Majeed, I.; Malik, R.N.; Iqbal, M.; Nadeem, M.A.; Hussain, I.; Yousaf, S.; Zeshan; Mustafa, G.; Zafar, M.I.; et al. Photocatalytic degradation of textile dyes on Cu₂O-CuO/TiO₂ anatase powders. *J. Environ. Chem. Eng.* **2016**, *4*, 2138–2146. [[CrossRef](#)]
12. Chauhan, A.; Sharma, M.; Kumar, S.; Thirumalai, S.; Kumar, R.V.; Vaish, R. TiO₂@C core@shell nanocomposites: A single precursor synthesis of photocatalyst for efficient solar water treatment. *J. Hazard. Mater.* **2020**, *381*, 2019. [[CrossRef](#)] [[PubMed](#)]
13. Mortazavian, S.; Saber, I.; James, D.E. Optimization of Photocatalytic Degradation of Acid Suspension System: Application of Response Surface. *Catalysts* **2019**, *9*, 360. [[CrossRef](#)]
14. Rizzo, L.; della Sala, A.; Fiorentino, A.; Puma, G.L. ScienceDirect Disinfection of urban wastewater by solar driven and UV lamp e TiO₂ photocatalysis: Effect on a multi drug resistant Escherichia coli strain. *Water Res.* **2014**, *53*, 145–152. [[CrossRef](#)]
15. Teh, C.M.; Mohamed, A.R. Roles of titanium dioxide and ion-doped titanium dioxide on photocatalytic degradation of organic pollutants (phenolic compounds and dyes) in aqueous solutions: A review. *J. Alloys Compd.* **2011**, *509*, 1648–1660. [[CrossRef](#)]
16. Wang, H.; Zhang, L.; Chen, Z.; Hu, J.; Li, S. Semiconductor heterojunction photocatalysts: Design, construction, and photocatalytic. *Chem. Soc. Rev.* **2014**, *43*, 5234–5244. [[CrossRef](#)]
17. Junwang, S. Visible-light driven heterojunction photocatalysts for water splitting—A critical review. *Energy Environ. Sci.* **2015**, *8*, 731–759. [[CrossRef](#)]
18. Gong, S.; Jiang, Z.; Zhu, S. enhanced visible-light photocatalytic activities heterojunctions with enhanced visible-light photocatalytic activities. *J. Nanopart. Res.* **2018**, *20*, 310. [[CrossRef](#)]
19. Hou, W.; Cronin, S.B. A review of surface plasmon resonance-enhanced photocatalysis. *Adv. Funct. Mater.* **2013**, *23*, 1612–1619. [[CrossRef](#)]
20. Liu, C.; Mao, S.; Wang, H.; Wu, Y.; Wang, F.; Xia, M.; Chen, Q. Peroxymonosulfate-assisted for facilitating photocatalytic degradation performance of 2D/2D WO₃/BiOBr S-scheme heterojunction. *Chem. Eng. J.* **2022**, *430*, 2021. [[CrossRef](#)]
21. Caudillo-Flores, U.; Muñoz-Batista, M.J.; Luque, R.; Fernández-García, M.; Kubacka, A. g-C₃N₄/TiO₂ composite catalysts for the photo-oxidation of toluene: Chemical and charge handling effects. *Chem. Eng. J.* **2019**, *378*, 122228. [[CrossRef](#)]
22. Jiang, X.H.; Xing, Q.J.; Luo, X.B.; Li, F.; Zou, J.P.; Liu, S.S.; Li, X.; Wang, X.K. Simultaneous photoreduction of Uranium(VI) and photooxidation of Arsenic(III) in aqueous solution over g-C₃N₄/TiO₂ heterostructured catalysts under simulated sunlight irradiation. *Appl. Catal. B Environ.* **2018**, *228*, 29–38. [[CrossRef](#)]
23. Luan, S.; Qu, D.; An, L.; Jiang, W.; Gao, X.; Hua, S.; Miao, X.; Wen, Y.; Sun, Z. Enhancing photocatalytic performance by constructing ultrafine TiO₂ nanorods/g-C₃N₄ nanosheets heterojunction for water treatment. *Sci. Bull.* **2018**, *63*, 683–690. [[CrossRef](#)]
24. Miranda, C.; Mansilla, H.; Yáñez, J.; Obregón, S.; Colón, G. Improved photocatalytic activity of g-C₃N₄/TiO₂ composites prepared by a simple impregnation method. *J. Photochem. Photobiol. A Chem.* **2013**, *253*, 16–21. [[CrossRef](#)]
25. Kočí, K.; Reli, M.; Troppová, I.; Šihor, M.; Kupková, J.; Kustrowski, P.; Praus, P. Photocatalytic decomposition of N₂O over TiO₂/g-C₃N₄ photocatalysts heterojunction. *Appl. Surf. Sci.* **2017**, *396*, 1685–1695. [[CrossRef](#)]
26. Li, J.; Liu, Y.; Li, H.; Chen, C. Fabrication of g-C₃N₄/TiO₂ composite photocatalyst with extended absorption wavelength range and enhanced photocatalytic performance. *J. Photochem. Photobiol. A Chem.* **2016**, *317*, 151–160. [[CrossRef](#)]
27. Zhou, B.; Hong, H.; Zhang, H.; Yu, S.; Tian, H. Heterostructured Ag/g-C₃N₄/TiO₂ with enhanced visible light photocatalytic performances. *J. Chem. Technol. Biotechnol.* **2019**, *94*, 3806–3814. [[CrossRef](#)]
28. Liu, C.; Mao, S.; Shi, M.; Hong, X.; Wang, D.; Wang, F.; Xia, M.; Chen, Q. Enhanced photocatalytic degradation performance of BiVO₄/BiOBr through combining Fermi level alteration and oxygen defect engineering. *Chem. Eng. J.* **2022**, *449*, 137757. [[CrossRef](#)]
29. Ranjithkumar, R.; Lakshmanan, P.; Devendran, P.; Nallamuthu, N.; Sudhahar, S.; Kumar, M.K. Investigations on effect of graphitic carbon nitride loading on the properties and electrochemical performance of g-C₃N₄/TiO₂ nanocomposites for energy storage device applications. *Mater. Sci. Semicond. Process.* **2021**, *121*, 105328. [[CrossRef](#)]
30. Liu, Y.; Wu, S.; Liu, J.; Xie, S.; Liu, Y. Synthesis of g-C₃N₄/TiO₂ nanostructures for enhanced photocatalytic reduction of U(vi) in water. *RSC Adv.* **2021**, *11*, 4810–4817. [[CrossRef](#)]
31. Kumar, V.; Avisar, D.; Betzalel, Y.; Mamane, H. Rapid visible-light degradation of EE2 and its estrogenicity in hospital wastewater by crystalline promoted g-C₃N₄. *J. Hazard. Mater.* **2020**, *398*, 122880. [[CrossRef](#)]
32. Zhao, S.; Chen, S.; Yu, H.; Quan, X. G-C₃N₄/TiO₂ hybrid photocatalyst with wide absorption wavelength range and effective photogenerated charge separation. *Sep. Purif. Technol.* **2012**, *99*, 50–54. [[CrossRef](#)]
33. Zhang, Y.; Thomas, A.; Antonietti, M.; Wang, X. Activation of carbon nitride solids by protonation: Morphology changes, enhanced ionic conductivity, and photoconduction experiments. *J. Am. Chem. Soc.* **2009**, *131*, 50–51. [[CrossRef](#)] [[PubMed](#)]
34. Li, C.; Sun, Z.; Xue, Y.; Yao, G.; Zheng, S. A facile synthesis of g-C₃N₄/TiO₂ hybrid photocatalysts by sol-gel method and its enhanced photodegradation towards methylene blue under visible light. *Adv. Powder Technol.* **2016**, *27*, 330–337. [[CrossRef](#)]

35. Li, J.; Wu, X.; Pan, W.; Zhang, G.; Chen, H. Vacancy-Rich Monolayer BiO_{2-x} as a Highly Efficient UV, Visible, and Near-Infrared Responsive Photocatalyst. *Angew. Chemie—Int. Ed.* **2018**, *57*, 491–495. [[CrossRef](#)] [[PubMed](#)]
36. Tang, Q.; Meng, X.; Wang, Z.; Zhou, J.; Tang, H. In Situ Microwave-Assisted Synthesis of Porous N-TiO₂/g-C₃N₄ Heterojunctions with Enhanced Visible-Light Photocatalytic Properties. *Appl. Surf. Sci.* **2018**, *430*, 253–262. [[CrossRef](#)]
37. Ren, H.T.; Liang, Y.; Han, X.; Liu, Y.; Wu, S.H.; Bai, H.; Jia, S.Y. Photocatalytic oxidation of aqueous ammonia by Ag₂O/TiO₂ (P25): New insights into selectivity and contributions of different oxidative species. *Appl. Surf. Sci.* **2020**, *504*, 2019. [[CrossRef](#)]
38. Ishibashi, K.I.; Fujishima, A.; Watanabe, T.; Hashimoto, K. Detection of active oxidative species in TiO₂ photocatalysis using the fluorescence technique. *Electrochem. Commun.* **2000**, *2*, 207–210. [[CrossRef](#)]
39. Wen, J.; Li, X.; Liu, W.; Fang, Y.; Xie, J.; Xu, Y. Photocatalysis fundamentals and surface modification of TiO₂ nanomaterials. *Cuihua Xuebao Chin. J. Catal.* **2015**, *36*, 2049–2070. [[CrossRef](#)]
40. Adly, M.S.; El-Dafrawy, S.M.; El-Hakam, S.A. Application of nanostructured graphene oxide/titanium dioxide composites for photocatalytic degradation of rhodamine B and acid green 25 dyes. *J. Mater. Res. Technol.* **2019**, *8*, 5610–5622. [[CrossRef](#)]

Disclaimer/Publisher’s Note: The statements, opinions and data contained in all publications are solely those of the individual author(s) and contributor(s) and not of MDPI and/or the editor(s). MDPI and/or the editor(s) disclaim responsibility for any injury to people or property resulting from any ideas, methods, instructions or products referred to in the content.